

# Relation between the intrinsic and observed central engine activity time: implications for ultra-long GRBs

He Gao<sup>1,2,3</sup>, Peter Mészáros<sup>1,2,3</sup>

<sup>1</sup>*Department of Astronomy and Astrophysics, Pennsylvania State University, 525 Davey Laboratory, University Park, PA 16802: hug18@psu.edu*

<sup>2</sup>*Department of Physics, Pennsylvania State University, 525 Davey Laboratory, University Park, PA 16802*

<sup>3</sup>*Center for Particle and Gravitational Astrophysics, Institute for Gravitation and the Cosmos, Pennsylvania State University, 525 Davey Laboratory, University Park, PA 16802*

## ABSTRACT

The gamma-ray burst (GRB) central engine intrinsic activity time  $T_{ce}$  is usually described through either the  $\gamma$ -ray duration  $T_{90}$  or through a generalized burst duration  $t_{burst}$  which includes both the  $\gamma$ -ray emission and (when present) an extended flaring X-ray plateau. Here, we define a more specific operational description of  $T_{ce}$ , and within the framework of the internal-external shock model, we develop a numerical code to study the relationship between  $T_{90}$  and  $T_{ce}$ , as well as between  $t_{burst}$  and  $T_{ce}$ , for different initial conditions. We find that when  $T_{ce} \lesssim 10^4$  s, late internal collisions or refreshed external collisions result in values of  $T_{90}$  and  $t_{burst}$  larger than  $T_{ce}$ , usually by factors of 2 – 3. For  $T_{ce} \gtrsim 10^4$  s, the  $t_{burst}$  is always a good estimator for  $T_{ce}$ , while  $T_{90}$  can underpredict  $T_{ce}$  when the late central engine activity is moderate. We find a clear bimodal distribution for  $T_{ce}$ , based on our simulations as well as on the observational data for  $T_{90}$  and  $t_{burst}$ . We suggest that  $t_{burst}$  is a reliable measure for defining “ultra-long” GRBs. Bursts with  $T_{90}$  of order  $10^3$  s need not belong to a special population, while bursts with  $t_{burst} > 10^4$  s, where the late central engine activity is more moderate and shows up in X-rays, may represent a new population. These conclusions are insensitive to the initial conditions assumed in the models.

## 1. INTRODUCTION

After decades of study, our knowledge of the progenitor for gamma-ray bursts (GRBs) is still limited due to the lack of direct observational constraints (e.g., Zhang 2011). In the CGRO/BATSE era, people suggested that the observed temporal behavior of GRB prompt

emission essentially reflects the temporal behavior of the central engine (Rees & Mészáros 1994; Kobayashi et al. 1997), which might provide clues about the progenitor. GRBs were classified into two categories: long-duration, soft-spectrum class (LGRBs) and the short-duration, hard-spectrum class (SGRBs), based on the bimodal distribution of GRBs in the duration-hardness diagram (Kouveliotou et al. 1993). Different type of progenitor were invoked for these two different class, i.e., core collapse from Wolf-Rayet star for LGRBs (Woosley 1993; Paczyński 1998; MacFadyen & Woosley 1999; Woosley & Bloom 2006) and mergers of two compact stellar objects (NS-NS and NS-BH systems) for SGRBs (Paczynski 1986; Eichler et al. 1989; Paczyński 1991; Narayan et al. 1992). Later observational results, such as the host galaxies types for each class, the supernova association identification for nearby GRBs, the localization of the burst with respect to their host galaxy, etc (Berger 2014, for a review), seems to support such interpretations for the progenitor.

Recently, a number of GRBs (GRBs 101225A, 111209A, 121027A and 130925A) have attracted attention due to their unusually long prompt duration ( $\sim$  hours instead of tens of seconds) compared to typical GRBs (Levan et al. 2014; Gendre et al. 2013; Virgili et al. 2013; Stratta et al. 2013), where “prompt” refers to the initial emission phase, before the afterglow proper. It is worth noting that these “ultra-long” GRBs are not the only cases, similar ones were also seen historically in BATSE and Konus-Wind data (e.g. Connaughton et al. 1997; Connaughton 1998, 2002; Giblin et al. 2002; Nicastro et al. 2004; Levan et al. 2005; Pal’shin et al. 2008). In these references, the “ultra-long” GRBs were defined based on their  $\gamma$ -ray duration  $T_{90}$ , when  $T_{90}$  is comparable or even larger than  $10^3$  s<sup>1</sup>. Some authors (Gendre et al. 2013; Nakauchi et al. 2013; Levan et al. 2014) proposed that these “ultra-long” GRBs may issue from a new type of progenitor stars with much larger radii, such as blue supergiants (Mészáros & Rees 2001; Nakauchi et al. 2013), which could naturally explain their unusually long durations.

However, it has been widely argued that the  $\gamma$ -ray duration is not a good reflection of the intrinsic central engine activity  $T_{ce}$ , since *Swift* observations suggest that many GRBs have an extended central engine activity time, manifested through flares (Burrows et al. 2005a; Zhang et al. 2006; Margutti et al. 2011) and extended shallow plateaus (Troja et al. 2007; Liang et al. 2007) in the X-ray light curves following the MeV emission. Most recently, Zhang et al. (2014) performed a comprehensive study on a large sample of *Swift* GRBs, in which they redefined the burst duration as  $t_{burst}$ , based on both  $\gamma$ -ray and the above X-ray light curve features. They found that within their “good” sample, 21.9% GRBs have  $t_{burst} \gtrsim 10^3$  s and 11.5% GRBs have  $t_{burst} \gtrsim 10^4$  s. They showed that GRBs with exceedingly

---

<sup>1</sup>Although no clear boundary line has been defined yet.

long  $t_{\text{burst}}$  do not necessarily have unusual  $T_{90}$  and those four traditional “ultra-long” GRBs are not among the longest ones although they do have relatively long  $t_{\text{burst}}$  ( $> 10^4$  s). They conclude that, in the sense of  $t_{\text{burst}}$ , the existing evidence is inadequate to separate those traditional “ultra-long” bursts from a new population. Interestingly, there is an apparent bimodal distribution of  $t_{\text{burst}}$  in their results, separating around  $10^4$  s (see their Fig 5). Although they claimed some selection effects that may strongly affect the distribution, the effects only apply to the first component ( $< 10^4$  s). Therefore, based on  $t_{\text{burst}}$ , the second component (distributed from  $10^4 \sim 10^6$  s) might be a real population that points toward a new type of progenitors.

Compared to  $T_{90}$ , which refers purely to MeV-range emission,  $t_{\text{burst}}$  has the advantage of better reflecting  $T_{\text{ce}}$ , especially when late activity becomes more moderate. However, late time features need not necessarily be related to late central engine activity, since they might be due to the late internal collisions or refreshed external collisions (Rees & Mészáros 1998; Sari & Mészáros 2000) from early ejected shells. Therefore in some cases,  $t_{\text{burst}}$  might overestimate  $T_{\text{ce}}$ . Before deciding whether  $T_{90}$  or  $t_{\text{burst}}$  should be used to define “ultra-long” bursts, or determining whether the “ultra-long” GRBs indeed require a new type of progenitor, it is crucial to gain a better understanding of the real distribution of  $T_{\text{ce}}$ .

Here we develop a numerical method to study the behavior of the ratios  $T_{90}/T_{\text{ce}}$  and  $t_{\text{burst}}/T_{\text{ce}}$  within the framework of the internal plus external shock (Rees & Mészáros 1994; Mészáros & Rees 1997; Kobayashi et al. 1997; Maxham & Zhang 2009; Gao et al. 2013). We estimate the distribution of  $T_{\text{ce}}$  using Monte Carlo simulations based on our models and on the observational data on the  $T_{90}$  distribution of all *Swift* GRBs<sup>2</sup> and the data on the  $t_{\text{burst}}$  distribution from Zhang et al. (2014). To better understand the intrinsic features of the ratios  $T_{90}/T_{\text{ce}}$  and  $t_{\text{burst}}/T_{\text{ce}}$ , the values of  $T_{90}$  and  $t_{\text{burst}}$  in the rest frame are essential. On the other hand, when estimating  $T_{\text{ce}}$  by comparing with observational results of  $T_{90}$  and  $T_{\text{burst}}$ , the redshift correction should be considered. The paper is structured as follows: in section 2, we describe our numerical method for estimating  $T_{90}$  and  $t_{\text{burst}}$  in the framework of the internal plus external shock model. The simulation details for obtaining realizations of our method are illustrated in section 3. We present the results for  $T_{90}/T_{\text{ce}}$  and  $t_{\text{burst}}/T_{\text{ce}}$  under different initial conditions, as well as the estimation for distribution of  $T_{\text{ce}}$  in section 4. We discuss our method and the results in Section 5. For convenience, we collect the definition of the various timescales in Table 1. Note that henceforth, in the rest of the manuscript, the redshift correction term  $((1+z)^{-1})$  for the timescales in the observer frame is omitted in all relevant formulae, for the sake of brevity.

---

<sup>2</sup>These data are collected from the website: <http://swift.gsfc.nasa.gov/archive/>

## 2. Method description

In the internal plus external shock model, a relativistic unsteady outflow is generated from the central engine within the ejection time  $T_{\text{ej}}$  (Rees & Mészáros 1994), which produces highly time-variable shocks lying inside the external blast wave radius. For simplicity, the outflow can be represented as a succession of shells ejected with random values of the Lorentz factor, mass and width. Due to nonuniformities in the velocity, mechanical collisions between adjacent shells occur, and a certain fraction of the relative kinetic energy is converted into internal energy by the resulting internal shocks. The internal energy thus generated is then radiated via synchrotron or inverse Compton scattering giving rise to the prompt  $\gamma$ -ray emission. We will call such collisions “effective collisions” when they produce detectable radiation. There are two timescales in the lab frame to describe the collision history,  $T_{\text{col,lab}}$  for the last mechanical collision, and  $T_{\text{eff,lab}}$  for the last effective collision, where  $T_{\text{col,lab}} \geq T_{\text{eff,lab}}$ . Their values in the observer frame are denoted  $T_{\text{col}}$  and  $T_{\text{eff}}$ . Besides internal collisions, the outermost shell will also interact with the external ambient medium, sweeping up an increasing amount of matter, which leads to its eventually slowing down. The trailing shells may collide with each other before interacting with the leading shell, but it is also possible that they collide against the leading decelerating shell (or shells) before they have undergone internal collisions, which confines the possible values of  $T_{\text{col}}$  and  $T_{\text{eff}}$ .

In previous numerical studies (Kobayashi et al. 1997; Maxham & Zhang 2009)  $T_{\text{col}}$  has been usually taken to be the prompt emission duration  $T_{90}$  (see section 5 for a detailed discussion about the difference between this work and previous works). As a better definition, we propose to use  $T_{\text{eff}}$  to represent  $T_{90}$ , taking also into account the detector properties for the detectability. Specifically, we use three criteria to define “effective internal collisions for  $\gamma$ -rays” : firstly the Lorentz factor ratio between two shells should be nominally  $\gtrsim 2$  (Rees & Mészáros 1994)<sup>3</sup>; secondly the peak radiation luminosity should be larger than the  $\gamma$ -ray detector sensitivity  $L_{\text{det},\gamma}$ ; and finally, the peak photon energy  $E_p$  should be within the  $\gamma$ -ray detector energy band. The final estimated prompt emission duration is denoted as  $T_{\text{pr,obs}}$ , where  $T_{\text{pr,obs}} \leq T_{\text{eff}}$ .

When the leading shell sweeping up enough matter, its kinetic energy is converted into afterglow emission via external shock (Mészáros & Rees 1997). Although the afterglow timescale is no longer connected with  $T_{\text{ej}}$ , if “effective internal collisions for X-rays” happen after the onset of the afterglow emission, or if energetic late shells collide onto the external blastwave (effective refreshed collisions), then we expect observable signatures such as flares

---

<sup>3</sup>This is a somewhat ad-hoc criterion, which in a more careful analysis could be loosened, but which qualitatively serves our immediate purposes here.

or plateaus, which may be detected superposed on the external shock afterglow signals (at time  $T_{\text{af}}$ ). In this case, the central engine timescale inferred from the observations should be  $T_{\text{ce,obs}} = \max(T_{\text{pr,obs}}, T_{\text{af}})$ . In Zhang et al. (2014) the X-ray light curve was fitted with a multi-segment broken power-law and  $T_{\text{burst}}$  was identified as the maximum of the steep (decay slope steeper than  $-3$ ) to shallow transition time. In our model,  $T_{\text{af}}$  is defined as the time when the last effective internal collision for X-rays or the last effective refreshed shock collision happens. The criterion for an effective internal collision for X-rays is similar to that for  $\gamma$ -rays, but the X-ray detector properties are used. For an effective refreshed collision, the collision needs to be violent, or else the injection energy needs to be comparable to impulsive energy in the initial blastwave if the collision is mild<sup>4</sup> (Zhang & Mészáros 2002). Although the definition of  $T_{\text{ce,obs}}$  is not fully equivalent with  $t_{\text{burst}}$ , for a large enough sample, it should be adequate to represent the overall distribution feature of  $t_{\text{burst}}$ .

In principle, given the initial conditions, i.e., the Lorentz factor, mass and width of the shells, the ejection time intervals between shells and the ambient medium density, the dynamical processes in the system can be precisely described through the numerical simulations. This allows us to study the expected values of the ratios  $T_{\text{pr,obs}}/T_{\text{ej}}$  and  $T_{\text{ce,obs}}/T_{\text{ej}}$  in our model, which essentially represent the ratios  $T_{90}/T_{\text{ce}}$  and  $t_{\text{burst}}/T_{\text{ce}}$  between the observed and the model-intrinsic features. These, in turn, provide an estimate of the intrinsic distributions of the  $T_{\text{ce}}$ , based on the observed values of  $T_{90}$  and  $t_{\text{burst}}$ .

### 3. Simulation Details

#### 3.1. Two Shell Interaction

The treatment of the two shell interaction is the basic element of this simulation. Most of the interactions are internal collisions between two adjacent shells. Only the interaction between the first and second shell should be treated differently when the first shell enters the deceleration phase, which is referred to as a refreshed collision (Rees & Mészáros 1998; Sari & Mészáros 2000).

---

<sup>4</sup>For a violent collision, a significant X-ray/optical flare would be produced, which could be easy to identify. For a mild collision, a shallow decay phase may appear in the afterglow light curve; however, to make it detectable, one would need  $\delta t_{\text{obs}}/t_{\text{col,obs}} = E_2/E_1$  to be of order unity (see section 3.1.2), i.e., the injection energy should be comparable to the initial blastwave energy. The criteria for violent collisions are defined later in section 3.1.2.

### 3.1.1. Internal Collision

Consider a rapid shell (at  $R_r$ ) with initial width  $l_r$ , Lorentz factor  $\gamma_r$  and mass  $m_r$ , chasing a slower shell (at  $R_s$ ), which has an initial width  $l_s$ , Lorentz factor  $\gamma_s$  and mass  $m_s$ . In the lab frame, the shells will collide after

$$t_{\text{col}} = \frac{R_s - R_r}{(\beta_r - \beta_s)c}, \quad (1)$$

at

$$R_{\text{col}} = \frac{\beta_r R_s - \beta_s R_r}{(\beta_r - \beta_s)}. \quad (2)$$

For simplicity, we assume the system behaves like an inelastic collision, so the two shells will merge to form a single new shell of width  $l_m$ , Lorentz factor  $\gamma_m$  and mass  $m_m$ . Using conservation of mass, energy and momentum, we can estimate the mass and Lorentz factor of the merged shell as

$$m_m = m_r + m_s \quad (3)$$

$$\gamma_m \simeq \sqrt{\frac{m_r \gamma_r + m_s \gamma_s}{m_r / \gamma_r + m_s / \gamma_s}}, \quad (4)$$

Based on a detailed hydrodynamic calculation, Kobayashi et al. (1997) proposed to estimate the width of merged shell as

$$l_m = l_s \frac{\beta_{fs} - \beta_m}{\beta_{fs} - \beta_s} + l_r \frac{\beta_m - \beta_{rs}}{\beta_r - \beta_{rs}}. \quad (5)$$

where  $\beta_{fs}$  is the speed of the forward shock propagating into the slow shell and  $\beta_{rs}$  is the speed of the reverse shock propagating into the fast shell. Their corresponding Lorentz factors are

$$\gamma_{fs} \simeq \gamma_m \sqrt{\left(1 + \frac{2\gamma_m}{\gamma_s}\right) / \left(2 + \frac{\gamma_m}{\gamma_s}\right)}, \quad \gamma_{rs} \simeq \gamma_m \sqrt{\left(1 + \frac{2\gamma_m}{\gamma_r}\right) / \left(2 + \frac{\gamma_m}{\gamma_r}\right)}. \quad (6)$$

The internal energy of the merged shell is the difference between the kinetic energy before and after the collision:

$$E_{\text{int}} = m_r c^2 (\gamma_r - \gamma_m) + m_s c^2 (\gamma_s - \gamma_m). \quad (7)$$

We define a free parameter  $f$  as the fraction of the internal energy emitted in the detector energy band. The emission time scale (in the lab frame) can be estimated as the time taken by the reverse shock to cross the rapid shell:

$$\delta t_e = \Delta_r / c (\beta_r - \beta_{rs}). \quad (8)$$

where  $\Delta_r$  is the width of the rapid shell, and

$$\Delta_r = \begin{cases} l_r, & R < R_{s,r} \\ \frac{R}{\gamma_r^2}, & R > R_{s,r}. \end{cases} \quad (9)$$

where  $R_{s,r} \sim \gamma_r^2 l_r$  is the spreading radius of the rapid shell. The peak luminosity for this collision can thus be expressed as

$$L_p = E_{\text{int}} f c (\beta_r - \beta_{rs}) / \Delta_r \quad (10)$$

We assume that the energy  $E_p$  of the spectral peak of the radiation can be estimated through the Amati relation, which is an empirical relation between the isotropic emission energy  $E_{\text{iso}}$  and  $E_p$ , generally valid among GRBs (Amati et al. 2002; Krimm et al. 2009) and also within a single burst (Liang et al. 2004; Ghirlanda et al. 2009). Here, we will assume the validity of this correlation for all effective internal collisions, and apply the relation  $E_{\text{iso}} = f E_{\text{int}}$  to estimate  $E_p$  as (Maxham & Zhang 2009)

$$E_p = \frac{100 \text{ keV}}{1+z} \left( \frac{E_{\text{iso}}}{10^{52} \text{ erg}} \right)^{1/2}. \quad (11)$$

In this work, the detector sensitivities adopted are those of the *Swift* BAT and XRT instruments. For BAT, the detector threshold is taken to be  $L_{\text{det},\gamma} = 10^{-8} \text{ erg s}^{-1} \text{ cm}^{-2}$ , and the energy band is 15 – 350 keV (Barthelmy et al. 2005; Maxham & Zhang 2009). For XRT, the sensitivity curve adopted is a broken power-law shape, with  $\propto t^{-1}$  early on, which breaks to  $\propto t^{-1/2}$  when  $F_\nu = 2.0 \times 10^{-15} \text{ erg cm}^{-2} \text{ s}^{-1}$  at  $t = 105 \text{ s}$ . The energy band is 0.2 – 10 keV (Burrows et al. 2005b; Moretti et al. 2009). These, together with the criteria discussed in section 2, are used to label a collision as an effective collision for  $\gamma$ -rays, an effective collision for X-rays, or as not effective.

After the collision, the remaining internal energy  $(1-f) * E_{\text{int}}$  converts back into kinetic energy. In the following simulations, instead of considering the reacceleration details, we simply correct the bulk Lorentz factor of the merged shell to account for this energy conversion. We also tested situations where this effect is neglected, and it turned out that the final results were not affected. This could be due to the fact that the energy conversion efficiency for an individual internal collision is typically low, only (1-10)%.

### 3.1.2. Refreshed Shock Collisions

The outermost shell will eventually slow down due to an external shock as it sweeps up the ambient medium. During the initial interaction, a pair of shocks (forward and reverse)

propagate into the ambient medium and into the shell, respectively (Sari & Piran 1995). After the reverse shock crosses the shell, the blastwave enters a self-similar phase described by the Blandford McKee self-similar solution (Blandford & McKee 1976). The deceleration radius  $R_{\text{dec}}$  beyond which the inertia from the circumburst medium is large enough and the Lorentz factor of the blastwave starts to decrease as a power law with radius is, for a constant density external medium  $n_0$ , given by

$$R_{\text{dec}} = \left( \frac{3E}{2\pi n_0 m_p c^2 \gamma_0^2} \right)^{1/3} \quad (12)$$

where  $E$  and  $\gamma_0$  are the initial kinetic energy and Lorentz factor of the outermost shell. Entering the self-similar phase, the dynamics of the blast wave in the constant energy regime can be described as (Blandford & McKee 1976)

$$\gamma = \left( \frac{17E}{4^8 \pi n_0 m_p c^5 t^3} \right)^{1/8}, \quad R = \left( \frac{17Et}{\pi n_0 m_p c} \right)^{1/4}, \quad (13)$$

where  $t$  is measured in the observer frame.

When the outermost shell is inside  $R_{\text{dec}}$ , its collision with the second outermost shell can be taken as an internal collision (see section 3.1.1). Otherwise, the collision should be treated as a refreshed collision with the external shock. We denote the first outer shell with subscript 1 and the second outer shell with 2. The refreshed collision will happen at

$$R_{\text{col}} \approx \begin{cases} R_1 + [8\gamma_1^2(R_1 - R_2)R_1^3]^{1/4}, & \gamma_1 < \gamma_2 \\ R_1 \left(\frac{\gamma_2}{\gamma_1}\right)^{-2/3} + [8\gamma_1^2(R_1 - R_2)R_1^3]^{1/4}, & \gamma_1 > \gamma_2 \end{cases} \quad (14)$$

and the collision time is  $t_{\text{col}} = (R_{\text{col}} - R_2)/\beta_2 c$ . The detailed dynamics of such collision is complicated, involving three shocks and several distinct dynamical stages (Kumar & Piran 2000; Zhang & Mészáros 2002). For the purposes of this study, we adopt the following simple treatment: 1) after the complicated collision process and the relaxation stage (at  $R_f$ ), the merged shell evolves with an initial total energy  $E_1 + E_2$  and an initial Lorentz factor  $\max(\gamma_1, \gamma_2)$ ; 2) between  $R_{\text{col}}$  and  $R_f$ , the shell 2 was assumed to inject its energy into shell 1 with a constant luminosity, which gives  $R_f = R_{\text{col}}(1 + E_2/E_1)^{1/2}$ . Therefore, the duration of the emission in the observer frame can be estimated as

$$\delta t_{\text{obs}} = t_{\text{col,obs}} E_2/E_1 \quad (15)$$

where  $t_{\text{col,obs}}$  is the relevant value for  $R_{\text{col}}$  in the observer frame.

The collision can be classified as either violent or mild, depending on whether a strong shock forms at the discontinuity between two colliding shells, which requires two criteria:



1) the injected shell should move supersonically with respect to the leading shell; 2) the injected shell is energetic enough to further heat up the leading shell. Quantitatively the criteria read (noticing that the sound speed  $c_s \simeq c/\sqrt{3}$  for the leading shell):

$$\begin{aligned} \gamma_{12} &\geq 1.22 \\ (4\gamma_{12} + 3)(\gamma_{12} - 1) &> \frac{4E_1}{E_2} \left[ \min \left( 1, \frac{R}{R_{s,2}} \right) \right]^{-1}, \end{aligned} \quad (16)$$

where  $\gamma_{12} = 1/2(\gamma_1/\gamma_2 + \gamma_2/\gamma_1)$  is the relative Lorentz factor between shells 1 and 2, and  $R_{s,2}$  is the spreading radius of shell 2 (Zhang & Mészáros 2002). We label the violent collisions or mild collisions with  $E_2/E_1 \geq 1$  as effective refreshed collisions.

### 3.2. The Multiple Shell Model

Consider an outflow consisting of  $N$  shells. We assign an index  $i$ , ( $i = 1, N$ ) to each shell according to the order of the emission from the inner engine. Each shell is characterized by four variables: a Lorentz factor  $\gamma_i$ , a mass  $m_i$ , a width  $l_i$  and the radius  $R_i$ <sup>5</sup>. At this initial stage, the initial lab frame time is set to  $t_{\text{lab},0}$ .

There will be  $N - 1$  collisions between different shells and eventually only one shell will be left, considering the confinement imposed by the external shock blastwave. For the  $n$ th collision (at  $t_{\text{lab},n}$ ), we first find out all the groups of adjacent shells ordered with decreasing values of the Lorentz factor. We denote with an index  $j$  for the  $j$ th group and with an index  $s$  for the shells in each group ( $s = 1$  has the largest Lorentz factor). With our results from §3.1.1, we can estimate the collision time  $t_{j,s}$  for the  $s$  and  $s + 1$  shells in the  $j$ th group, and find the pair with the shortest  $t_{j,s}$  among all the groups, assigning it the label  $t_{\text{next}}^n$ . With the information of  $(j,s)$ , we can find the shell index of the next expected collision pair  $(h,h + 1)$ . Note that one needs to check whether the outermost shell is already in the deceleration phase or not. If so, the outermost shell and the second outer shell should always be treated as the  $j + 1$  group.

We then rearrange the shells as follows: for  $i \leq h$ , each shell moves from its earlier position  $R_i(t_{\text{lab},n-1})$  to

$$R_i(t_{\text{lab},n}) = R_i(t_{\text{lab},n-1}) + c\beta_i t_{\text{next}}^n. \quad (17)$$

---

<sup>5</sup>For specific simulations,  $R_i$  is calculated as  $R_i = r_0 + \beta_i c(\sum_i l_i/c + \sum_i \Delta t_{ej,i})$ , where  $\Delta t_{ej}$  is the ejection time interval between shells,  $r_0$  is the central engine radius, whose value does not affect the final results as long as it is smaller than  $c\Delta t_{ej,i}$ . In this work, we adopt  $r_0 = 10^7$ cm.

The  $i < h$  shells keep their other properties  $\gamma_i$ ,  $m_i$  and  $l_i$ , while  $i = h$  is the new merged shell with the new  $\gamma_h$ ,  $m_h$  and  $l_h$  calculated based on section 3.1.1 (or section 3.1.2 if the refreshed shock happen first). We delete the  $h + 1$  th shell. For  $i > h + 1$ , each shell's index is reduced by one, and has a new position

$$R_{i-1}(t_{\text{lab},n}) \equiv R_i(t_{\text{lab},n-1}) + c\beta_i t_{\text{next}}^n. \quad (18)$$

They also keep their other properties. We then return to the calculation of the  $(n+1)$  th step until all the shells have merged to form a single external blastwave, where the simulation stops.

In the lab frame, the  $n$ th collision would happen at

$$t_{\text{lab},n} = t_{\text{lab},0} + \sum_1^n t_{\text{next}}^n. \quad (19)$$

For an observer at a luminosity distance  $D_L$  from the central engine, the radiation from this collision would start to be detected at

$$t_n = (D_L - R_{\text{col},n})/c + t_{\text{lab},n}. \quad (20)$$

At the end of the simulation, we set the minimum of  $t_n$  to be the origin of the observer time, since this is when the source triggered the detector. We thus have

$$t_{\text{obs},n} = t_n - \min(t_1, t_2, \dots, t_{N-1}). \quad (21)$$

For internal collisions, the observer-frame emission duration  $\delta t_{\text{obs},n}$  is estimated as  $\delta t_{e,n}/2\gamma_m^2$ , where  $\gamma_m$  is the merged Lorentz factor for that collision. For refreshed collisions, we take  $\delta t_{\text{obs},n} = t_{\text{obs},n} \times (E_2/E_1)$ , where  $E_1$  is the blastwave energy and  $E_2$  is the subsequent injected energy for that collision. We search for the last effective internal collision for  $\gamma$ -rays (labelled as  $n\gamma$ ), the last effective internal collision for X-rays (labelled as  $nX$ ), and the last effective refreshed collision (labelled as  $nR$ ) in the observer frame, leading to

$$\begin{aligned} T_{\text{pr,obs}} &= t_{\text{obs},n\gamma} + \delta t_{\text{obs},n\gamma} \simeq T_{90}, \\ T_{\text{ce,obs}} &= \max(t_{\text{obs},n\gamma} + \delta t_{\text{obs},n\gamma}, t_{\text{obs},nX} + \delta t_{\text{obs},nX}, t_{\text{obs},nR} + \delta t_{\text{obs},nR}) \simeq t_{\text{burst}} \end{aligned} \quad (22)$$

### 3.3. Initial conditions

For each simulation, the initial conditions include the Lorentz factor, mass and width of the shells ( $\gamma$ ,  $m$  and  $l$ ), the ejection time intervals between shells ( $\Delta t_{\text{ej}}$ ), the ambient

medium density and the redshift of the source. In this work, we assume a constant density for the ambient medium, with  $n = 1 \text{ cm}^{-3}$ . For each simulation, the source redshift is simulated based on the observed  $z$  distribution of the observed GRBs<sup>6</sup> (see Figure 1(b) in Gao et al. (2014)). Other parameters are determined by the central engine, and these are very uncertain. We tested different distribution functions for each parameter, especially for the Lorentz factor of the shells and the shell ejection time interval, which are more crucial for determining the observable timescales. We allow for one quiescent period in the central engine activity, that is, the shells may be ejected within one episode, or within two episodes separated by  $T_{\text{quie}}$ . As a nominal case, we assume that 100 shells are ejected in each episode. The second episode can either share the same set of initial conditions as the first one, or it can be less energetic by assigning a lower mass to each shell. Details of the combinations of initial conditions are collected in Table 2, numbered as different models. Here RAN ( $\tilde{a}, \tilde{b}$ ) denotes a uniform distribution from  $\tilde{a}$  to  $\tilde{b}$ ; PL ( $\tilde{a}, \tilde{b}, \tilde{c}$ ) denotes a power-law distribution from  $\tilde{a}$  to  $\tilde{b}$  with index  $\tilde{c}$ ; GAUSS ( $\tilde{a}, \tilde{b}$ ) denotes a Gaussian distribution with a mean  $\tilde{a}$  and a standard deviation  $\tilde{b}$ .

The reason for selecting these models can be briefly summarized as follows: for one episode ejection, we assume that the plausible shell ejection time interval are distributed as RAN(0.5, 2.5), giving a total ejection timescale of  $\sim 100$ s for 100 shells. Concerning the Lorentz factor of the shells, we assume the most plausible parameters for each of the three distribution functions, e.g. RAN(50, 500), PL(100, 500,  $-0.5$ ) and GAUSS(300, 100), to ensure a mean value of the Lorentz factor of  $\sim 300$ . Furthermore, we assume the mass of the shells is distributed with a uniform distribution in log space  $10^{27} \sim 10^{29}$  g, giving a total energy of  $10^{52} \sim 10^{54}$ erg. These combined assumptions are used to propose what we consider to be the three most plausible models for the initial conditions of the GRB central engine, e.g. model 1 (RAN-type), 7 (PL-type) and 9 (GAUSS-type). To account for the variability of the central engine properties, other specific models are also considered. For instance, model 2 is for cases when the shells have higher average Lorentz factors; models 3, 8 and 10 are for cases when the total ejection timescale is  $\sim 1000$  s; models 11-22 are for two episode ejection cases, where the second episode has the same or is less energetic compared to the first one, and the separation timescale between the two ejections is  $10^3$  s or  $10^4$  s.

Note that for given model, the central engine activity time is calculated as

$$T_{\text{ej}} \equiv T_{\text{ce}} = \sum_i l_i/c + \sum_i \Delta t_{\text{ej},i} + T_{\text{quie}} \quad (23)$$

---

<sup>6</sup>The data was collected from an online catalog listed at <http://lyra.berkeley.edu/grbox/grbox.php>.

## 4. Results

### 4.1. Summary of the Numerical Results

For each model, we run the simulation 500 times <sup>7</sup>, and we analyze the thus obtained distributions of  $T_{\text{pr,obs}}/T_{\text{ej}}$  and  $T_{\text{ce,obs}}/T_{\text{ej}}$  in the rest frame. In Figure 1 we plot the results for selected models which are relevant for reflecting the main conclusions, which can be summarized as follows (for easy identification, Table 2 summarizes the corresponding subfigure numbers for the different models):

- When the initial  $\gamma$ 's of the shells are distributed from 500 to 1000, compared to the case when they are distributed from 50 to 500, both  $T_{\text{pr,obs}}/T_{\text{ej}}$  and  $T_{\text{ce,obs}}/T_{\text{ej}}$  have a much narrower distribution around unity in the former case, due to a stronger confinement from the external blast wave.
- Different distribution functions for the initial  $\gamma$ 's of shells affect only moderately the results. The RAN and GAUSS functions give very similar results as long as they have similar distribution ranges. The results for PL( $\tilde{a}, \tilde{b}, \tilde{c}$ ) are sensitive to the lower ending  $\tilde{a}$  and the index  $\tilde{c}$  of the distribution. Smaller  $\tilde{a}$  or  $\tilde{c}$  tends to give more spread-out distributions and larger maximum values for both  $T_{\text{pr,obs}}/T_{\text{ej}}$  and  $T_{\text{ce,obs}}/T_{\text{ej}}$ .
- When  $T_{\text{ej}}$  is of order of 100 s, the  $T_{\text{pr,obs}}/T_{\text{ej}}$  distribution has a sharp peak at unity, and a Gaussian-shape spreading from 0 to 2, depending on specific models.  $T_{\text{ce,obs}}/T_{\text{ej}}$  behaves as a FRED-like (fast rise exponential decay) distribution from 1 to less than 10, also depending on specific models.
- For one-episode injection cases, when  $T_{\text{ej}}$  is of order of 100 s,  $T_{\text{pr,obs}}/T_{\text{ej}}$  has an upper limit of order of 10, and  $T_{\text{ce,obs}}/T_{\text{ej}}$  has an upper limit of order of 100 (for most cases, the upper limit is also of order 10, except when  $\gamma$  has a PL distribution starting from 50). On the other hand, when  $T_{\text{ej}}$  is of order 1000 s,  $T_{\text{pr,obs}}/T_{\text{ej}}$  has a very narrow distribution within 0 – 2 and  $T_{\text{ce,obs}}/T_{\text{ej}}$  also has a relatively narrow distribution with an upper limit smaller than 10. These results indicate that for one-episode injection,  $T_{\text{pr,obs}}$  has an upper limit of order 1000 s, and  $T_{\text{ce,obs}}$  has an upper limit of order  $10^4$  s. These upper limits are set by the confinement of the blast wave and are model independent.

---

<sup>7</sup>The number of runs for each simulation is determined by balancing the computation time consumption and the resulting convergence.

- For two-episode injection cases, when the second episode is similar to the first one,  $T_{\text{pr,obs}}/T_{\text{ej}}$  has a very narrow distribution around unity, with some rare exceptions distributed around 0.1 (due to the high redshift). Also  $T_{\text{ce,obs}}/T_{\text{ej}}$  is mainly concentrated around unity, spreading up to 2 – 3. When the second episode is less energetic,  $T_{\text{pr,obs}}$  is essentially determined by the first episode, which has an upper limit of order 1000 s, and the  $T_{\text{ce,obs}}/T_{\text{ej}}$  is distributed narrowly around unity. In short,  $T_{\text{ce,obs}}$  reflects well the time  $T_{\text{ej}}$  during which the late central engine is active, whereas  $T_{\text{pr,obs}}$  can be much smaller than  $T_{\text{ej}}$ , if the later injection is less energetic.
- The overall internal collision efficiency (total internal energy created from internal collision divided by total energy of ejected shells) is distributed with a Gaussian shape. The peak value for the RAN and GAUSS models are around 30% – 40%, while the PL models are less efficient, with a peak around 15% – 30%.

#### 4.2. Distribution of the Intrinsic Central Engine Activity Timescale

In the above simulations,  $T_{\text{ce}}$  ( $T_{\text{ej}}$ ) are concentrated in a very narrow range, for a given model. In reality,  $T_{\text{ce}}$  should have a much wider distribution, in order to produce the observed distribution profiles of  $T_{90}$  ( $T_{\text{pr,obs}}$ ) and  $t_{\text{burst}}$  ( $T_{\text{ce,obs}}$ ). The observed distributions of  $T_{90}$  of all *Swift* bursts, and of  $t_{\text{burst}}$  in the good sample of Zhang et al. (2014), are plotted in Figure 2. With a better understanding about the relation between  $T_{90}$  and  $T_{\text{ce}}$ , and also between  $t_{\text{burst}}$  and  $T_{\text{ce}}$ , we can now provide a better estimate for  $T_{\text{ce}}$ .

Since  $t_{\text{burst}}$  becomes very close to  $T_{\text{ce}}$  when  $T_{\text{ce}} \gtrsim 10^4$  s, the second component in the  $t_{\text{burst}}$  distribution (from  $10^4 \sim 10^6$  s) should show a similar structure in the  $T_{\text{ce}}$  distribution. If we treat this late time activity as a second episode injection, it must be less energetic compared to the first one, since the  $T_{90}$  distribution lacks a corresponding excess. Based on the same argument, one continuous long episode is also ruled out. On the other hand, for the majority of cases when  $T_{\text{ce}} \lesssim 10^3$  s, both  $t_{\text{burst}}$  and  $T_{90}$  would be comparable to, or a slight overestimate of  $T_{\text{ce}}$ . Since both  $T_{90}$  and the first component for  $t_{\text{burst}}$  has a cutoff around  $10^3$  s, another component for  $T_{\text{ce}}$  is required, whose distribution profile should be similar to  $T_{90}$  and the first component of  $t_{\text{burst}}$ , but with an overall shift.

As a good representation of the observed distributions (the dashed lined histograms in Figure 2, we propose a Gaussian distribution for the first component of  $T_{\text{ce}}$  and a Gaussian distribution in log space for the second one (see Figure 2a). The population ratio between the two components is 5 : 1. We apply the simulation results of three plausible models, e.g., model 1 (RAN-type), 7 (PL-type) and 9 (GAUSS-type) to the first component. Moreover,

since the second component should be less energetic, we correspondingly apply the results of model 13 (RAN-type), 17 (PL-type) and 22 (GAUSS-type) to the second component. In principle, a distribution test could be used here to find out the best parameters for the  $T_{ce}$  distribution. Due to an incomplete understanding of the real  $T_{ce}$  distribution profile, and an incomplete understanding of relevant selection effects (Zhang et al. 2014), we only show in Figure 2 an example of a  $T_{ce}$  distribution that gives reasonable results for both  $T_{90}$  and  $t_{burst}$ , instead of using a distribution test to find out the best parameters.

In this example, the first component is a GAUSS(60, 80) and the second one is a GAUSS(4.5, 0.5) in log space. The results are shown in Figure 2. We find that the proposed  $T_{ce}$  distribution provides a good match to the observational results, and it is largely insensitive to the initial conditions of the internal-external shock models used. If our estimates are indeed as robust as they appear, the following implications can be inferred:

1) For the first component, our model  $T_{ce}$  is smaller than 300 s within  $3\sigma$ , and appears adequate to account for the rare observed tails of  $T_{90}$  which extend to over  $10^3$  s. This suggests that bursts with  $T_{90}$  of order of  $10^3$  s need not belong to a special population, and their relevant intrinsic central engine activity time may be even smaller than 300 s.

2) Unlike the distribution structure of  $t_{burst}$ , there is an obvious gap between the two components of  $T_{ce}$ , indicating a more clearly bimodal distribution. In this sense, bursts with  $t_{burst} > 10^4$  s might indeed belong to a new population, and it is more reliable to use  $t_{burst}$  to define “ultra-long” GRBs;

3) For the “ultra-long” GRBs defined by  $t_{burst}$ , the late central engine activity tends to be much more moderate than the early activity.

## 5. Discussion and Conclusions

Within the framework of the internal plus external shock model, we have developed a numerical code to study in greater detail the relationship between  $T_{90}$  and  $T_{ce}$ , as well as between  $t_{burst}$  and  $T_{ce}$ , for a range of different initial conditions.

In the literature, previous numerical simulations for internal shocks have been done, but aimed at different problems, e.g., testing the ability of internal shock models to produce the temporal variability (Kobayashi et al. 1997), studying the power density spectrum of GRB lightcurves in internal shock model (Panaitescu et al. 1999), studying the detailed radiation properties of internal shock models (Daigne & Mochkovitch 1998) and modeling the X-ray flares (Maxham & Zhang 2009). The main difference between our present study

and the previous ones is that we use both the internal collision shock properties and the real detector sensitivities to estimate the prompt duration; we consider the confinement imposed by the external blastwave to the late residual collisions<sup>8</sup>; for the first time, we use a detailed criterion to define effective refreshed collisions to calculate the observable central engine activity time; for the first time, we randomly generate all the initial condition parameters with many different distribution functions, intercomparing the results. Finally, since the real detector sensitivities are used, it is essential to assign a reasonable redshift to each simulated source for internal consistency. In this work, we rely on the actual observational GRB redshift distribution information rather than assuming one average redshift for all the sources, as has been done in some previous works. Such a treatment is also important when connecting intrinsic timescales in the rest frame with the corresponding values in the observer frame.

Some caveats about our numerical method and how these might affect the results are:

1) At the shell injection stage, we assume that the shell is released with relativistic speed, rather than considering the acceleration process for the shells. This should not affect our results since the acceleration phase should finish well below the internal shock radius.

2) We did not consider the details of the internal shock radiation. Here to estimate  $L_p$  we assumed that  $f = 0.5$ , i.e., 50% of the energy dissipated during collisions goes into radiation, and we used the Amati relation to calculate the spectral peak energy  $E_p$ . This value is adopted for keeping the overall radiation efficiency  $\eta_\gamma = E_\gamma/(E_\gamma + E_K)$  at 10% – 20%, where  $E_\gamma$  is the isotropic gamma-ray energy and  $E_K$  is the isotropic kinetic energy (Zhang et al. 2007). To justify this assumption, we re-simulated all the results by using  $f = 1$  (see pink lines in Figures 1). It turns out the results are almost independent on the  $f$  value, especially for  $T_{\text{ce,obs}}$ . The issue of whether  $f = 0.5$  (or  $f = 1$ ) might be too large in the sense of the electron equipartition energy fraction  $\epsilon_e$  would lead to the so-called “efficiency problem” for the internal shock model (Granot et al. 2006, and reference therein), which is out of the scope of this paper. However, it is still worth pointing out that the results in this work are also applicable to other internal collision relevant GRB models, such as the Internal- Collision-induced MAgnetic Reconnection and Turbulence (ICMART) model, which effectively increase the  $f$  value by invoking a more efficient radiation process (Zhang & Yan 2011).

3) When defining effective internal collisions for  $\gamma$ -rays, the results is dependent on the adopted detector sensitivity limit, since sometimes the late time internal collisions only give

---

<sup>8</sup>Note that the detector sensitivity and the blast wave refreshing by subsequent collisions were also considered in Maxham & Zhang (2009), when they estimate the observable features of X-ray flares.

marginally detectable signals. We justify this effect by decreasing  $L_{\text{det},\gamma}$  to  $10^{-9}$  erg s $^{-1}$  cm $^{-2}$  and re-simulate all the results for  $T_{\text{pr,obs}}$  (green lines in Figures 1). It turns out that the distribution of  $T_{\text{pr,obs}}$  becomes slightly more spread out for lower detector sensitivities, but does not affect our main conclusions above. Note that in a more precise treatment, the detailed detector trigger function would also be required (Levan et al. 2014).

4) When defining effective internal collisions for X-rays, we used an X-ray detector sensitivity limit as a threshold. In reality, one needs to compare the peak flux of the relevant X-ray flares with the baseline of X-ray afterglows from the external shock. We did not calculate the external shock afterglow lightcurves since too many additional unknown free parameters would be involved. This might only affect the results concerning  $T_{\text{ce,obs}}$  for very limited cases, i.e., one-episode injection cases and  $T_{\text{ce,obs}}$  are determined by weak residual internal collisions rather than refreshed collisions.

5) In the simulations, we assume a constant density for the circumburst medium, with  $n = 1$  cm $^{-3}$ . If the actual density baseline is different, the dynamics of the external blastwave and thus its confinement of the late internal collisions would be affected, although the dependence of the blastwave dynamics on the value of  $n$  is relatively small, as shown from equations 12 and 13. We have tested such effects through some additional simulation runs for four constant values of the circumburst number density, e.g.,  $n = 0.1$  cm $^{-3}$ ,  $n = 1$  cm $^{-3}$ ,  $n = 10$  cm $^{-3}$  and  $n = 100$  cm $^{-3}$ . It turns out that for specific models such as the plausible models 1, 7 and 9, the deviation among the results for the different number densities are less than a factor of 2 for both  $T_{\text{pr,obs}}/T_{\text{ej}}$  and  $T_{\text{ce,obs}}/T_{\text{ej}}$ . On the other hand, the medium density could be of a wind type instead of being constant. If so, the blastwave tends to start deceleration at a lower radius, which might lead to a stronger confinement of the late internal collisions. The consequences for our results of having such a wind can be estimated as follows. Since the blastwave confinement starts to work at the deceleration radius, bursts with similar values of  $R_{\text{dec}}$  and  $n(R_{\text{dec}})$  (the number density at  $R_{\text{dec}}$ ) should give similar results in our simulations, regardless of the exact density profile. For the commonly used free stratified wind model  $n = AR^{-2}$ , with  $A = \dot{M}/4\pi m_p v_w = 3 \times 10^{35} A_* \text{cm}^{-1}$  and  $A_* = (\dot{M}/10^{-5} M_\odot \text{yr}^{-1})(v_w/10^3 \text{km s}^{-1})^{-1}$  (Chevalier & Li 1999, 2000), the deceleration radius is  $R_{\text{dec}} = E/(2\pi A m_p c^2 \gamma_0^2)$ . Comparing with our equ.(12), we have  $R_{\text{dec}}^{\text{wind}}/R_{\text{dec}}^{\text{const}} = 1.1 E_{53}^{2/3} n_2^{1/3} A_{*, -1}^{-1} \gamma_{0,2}^{-4/3}$ , and  $n(R_{\text{dec}}^{\text{wind}})/n(R_{\text{dec}}^{\text{const}}) = 0.25 E_{53}^{-2} n_2^{-1} A_{*, -1}^3 \gamma_{0,2}^4$ . The results depend sensitively on the value of  $A_*$ , which is very uncertain due to our poor knowledge of the GRB progenitors, and in principle it could vary from 0.01 to 10 (Chevalier & Li 1999). One sees that for  $A_* < 1$  cases, as far as the confinement effect, the wind type medium should be comparable to a constant medium with  $n \sim 10^2$  cm $^{-3}$ , with the inference that for a wind medium, our results might be altered a factor of  $\sim 2$ . Although  $A_* \lesssim 1$  values are plausible, it is worth pointing out that more severe deviations might occur for a wind type medium if



$A_*$  is much larger than unity.

6) Within one ejection episode, the initial Lorentz factors of all shells, no matter whether earlier or later ejected, are chosen randomly out of certain distribution functions (RAN, PL or GAUSS). The temporal variability of the distribution is not considered, since this is related to the activity details of the GRB central engine, which is very uncertain, and at this point no numerical simulations have tackled this difficult problem yet. However, it is worth noting that if the distribution functions indeed suffer a temporal evolution, the present results could be altered. For instance, if the shells ejected later tend to have lower initial Lorentz factors, internal collisions would become inefficient or even nonoperational at the late stages, leading to smaller values of  $T_{\text{pr,obs}}$ . In this case, the value of  $T_{\text{ce,obs}}$  could become either smaller or larger, depending on whether the late ejected shells are energetic enough to trigger effective refreshed collisions.

7) When using the results of  $t_{\text{burst}}$  to estimate  $T_{\text{ce}}$ , a more careful treatment for the selection effects would give better results. Two types of selection effects are essential: 1) effects due to the satellite properties (Zhang et al. 2014); 2) effects due to the sample selection criteria defined in Zhang et al. (2014).

In summary, we find that late internal collisions or refreshed external collisions from early ejected shells result in values of  $T_{90}$  and  $t_{\text{burst}}$  larger than  $T_{\text{ce}}$ , usually by factors of 2–3. However this is only valid when  $T_{\text{ce}} \lesssim 10^4$  s, owing to the confinement by the external blastwave. For  $T_{\text{ce}} \gtrsim 10^4$  s cases,  $t_{\text{burst}}$  is always a good estimator for  $T_{\text{ce}}$ , and  $T_{90}$  might be much smaller than  $T_{\text{ce}}$  when the late central engine activity is moderate. These conclusions are insensitive to the initial condition assumed for the models. We have used the results of our simulations to estimate the intrinsic distribution of central engine activity times  $T_{\text{ce}}$ , making use of the observational data for  $T_{90}$  and  $t_{\text{burst}}$ . The results suggest a clear bimodal distribution of  $T_{\text{ce}}$ , a conclusion which is insensitive to the initial conditions used in the models. Based on these results, we conclude (i) that bursts with  $T_{90}$  of order of  $10^3$  s need not belong to a special population, and (ii) that their intrinsic central engine activity time could be substantially smaller than 300 s. Bursts with  $t_{\text{burst}} > 10^4$  s might, on the other hand, belong a new population, and  $t_{\text{burst}}$  appears to be a reliable measure to define “ultra-long” GRBs. Our results are also compatible with the late central engine activity of such bursts tending to become much more moderate than the early activity, as might be expected from a tapering off of the amount of fall-back material onto the central engine. Further observations and a larger sample of ultra-long GRBs will be required before firmer conclusions about this model can be drawn.

We thank Bing Zhang and Bin-Bin Zhang for helpful comments, and an anonymous ref-

eree for a constructive report. This research was supported in part by NASA NNX 13AH50G.

## REFERENCES

- Amati, L., Frontera, F., Tavani, M., et al. 2002, *A&A*, 390, 81
- Barthelmy, S. D., Barbier, L. M., Cummings, J. R., et al. 2005, *Space Sci. Rev.*, 120, 143
- Berger, E. 2014, *ARA&A*, 52, 43
- Blandford, R. D., & McKee, C. F. 1976, *Physics of Fluids*, 19, 1130
- Burrows, D. N., Romano, P., Falcone, A., et al. 2005a, *Science*, 309, 1833
- Burrows, D. N., Hill, J. E., Nousek, J. A., et al. 2005b, *Space Sci. Rev.*, 120, 165
- Chevalier, R. A., & Li, Z.-Y. 1999, *ApJ*, 520, L29
- Chevalier, R. A., & Li, Z.-Y. 2000, *ApJ*, 536, 195
- Connaughton, V., Kippen, R. M., Preece, R., & Hurley, K. 1997, *IAU Circ.*, 6785, 1
- Connaughton, V. 1998, *Eighteenth Texas Symposium on Relativistic Astrophysics*, 514
- Connaughton, V. 2002, *ApJ*, 567, 1028
- Daigne, F., & Mochkovitch, R. 1998, *MNRAS*, 296, 275
- Eichler, D., Livio, M., Piran, T., & Schramm, D. N. 1989, *Nature*, 340, 126
- Gao, H., Lei, W.-H., Zou, Y.-C., Wu, X.-F., & Zhang, B. 2013, *New A Rev.*, 57, 141
- Gao, H., Li, Z., & Zhang, B. 2014, *ApJ*, 788, 189
- Gendre, B., Stratta, G., & on behalf of the FIGARO collaboration 2013, *arXiv:1305.3194*
- Giblin, T. W., Connaughton, V., van Paradijs, J., et al. 2002, *ApJ*, 570, 573
- Ghirlanda, G., Nava, L., Ghisellini, G., Celotti, A., & Firmani, C. 2009, *A&A*, 496, 585
- Granot, J., Königl, A., & Piran, T. 2006, *MNRAS*, 370, 1946
- Kobayashi, S., Piran, T., & Sari, R. 1997, *ApJ*, 490, 92
- Kouveliotou, C., Meegan, C. A., Fishman, G. J., et al. 1993, *ApJ*, 413, L101

- Krimm, H. A., Yamaoka, K., Sugita, S., et al. 2009, *ApJ*, 704, 1405
- Kumar, P., & Piran, T. 2000, *ApJ*, 532, 286
- Levan, A., Nugent, P., Fruchter, A., et al. 2005, *ApJ*, 624, 880
- Levan, A. J., Tanvir, N. R., Starling, R. L. C., et al. 2014, *ApJ*, 781, 13
- Liang, E. W., Dai, Z. G., & Wu, X. F. 2004, *ApJ*, 606, L29
- Liang, E.-W., Zhang, B.-B., & Zhang, B. 2007, *ApJ*, 670, 565
- MacFadyen, A. I., & Woosley, S. E. 1999, *ApJ*, 524, 262
- Margutti, R., Bernardini, G., Barniol Duran, R., et al. 2011, *MNRAS*, 410, 1064
- Maxham, A., & Zhang, B. 2009, *ApJ*, 707, 1623
- Mészáros, P., & Rees, M. J. 2001, *ApJ*, 556, L37
- Mészáros, P., & Rees, M. J. 1997, *ApJ*, 476, 232
- Moretti, A., Pagani, C., Cusumano, G., et al. 2009, *A&A*, 493, 501
- Nakauchi, D., Kashiyama, K., Suwa, Y., & Nakamura, T. 2013, *ApJ*, 778, 67
- Narayan, R., Paczyński, B., & Piran, T. 1992, *ApJ*, 395, L83
- Nicastro, L., in't Zand, J. J. M., Amati, L., et al. 2004, *A&A*, 427, 445
- Paczynski, B. 1986, *ApJ*, 308, L43
- Paczynski, B. 1991, *Acta Astron.*, 41, 257
- Paczynski, B. 1998, *ApJ*, 494, L45
- Pal'shin, V., Aptekar, R., Frederiks, D., et al. 2008, *American Institute of Physics Conference Series*, 1000, 117
- Panaitescu, A., Spada, M., & Mészáros, P. 1999, *ApJ*, 522, L105
- Rees, M. J., & Mészáros, P. 1994, *ApJ*, 430, L93
- Rees, M. J., & Mészáros, P. 1998, *ApJ*, 496, L1
- Sari, R., & Piran, T. 1995, *ApJ*, 455, L143

- Sari, R., & Mészáros, P. 2000, *ApJ*, 535, L33
- Stratta, G., Gendre, B., Atteia, J. L., et al. 2013, *ApJ*, 779, 66
- Troja, E., Cusumano, G., O’Brien, P. T., et al. 2007, *ApJ*, 665, 599
- Virgili, F. J., Mundell, C. G., Pal’shin, V., et al. 2013, *ApJ*, 778, 54
- Woosley, S. E. 1993, *ApJ*, 405, 273
- Woosley, S. E., & Bloom, J. S. 2006, *ARA&A*, 44, 507
- Zhang, B.-B., Zhang, B., Murase, K., Connaughton, V., & Briggs, M. S. 2014, *ApJ*, 787, 66
- Zhang, B., & Mészáros, P. 2002, *ApJ*, 566, 712
- Zhang, B., Fan, Y. Z., Dyks, J., et al. 2006, *ApJ*, 642, 354
- Zhang, B., Liang, E., Page, K. L., et al. 2007, *ApJ*, 655, 989
- Zhang, B. 2011, *Comptes Rendus Physique*, 12, 206
- Zhang, B., & Yan, H. 2011, *ApJ*, 726, 90

Symbol	Definition
$T_{ce}$	Intrinsic central engine activity timescale
$T_{90}$	Time interval over which 90% of the total background-subtracted counts are observed in $\gamma$ -ray band
$t_{burst}$	Burst duration defined based on both $\gamma$ -ray and the X-ray light curve features (Zhang et al. 2014)
$T_{ej}$	Ejection timescale in the simulation, corresponding to $T_{ce}$ for real source
$T_{pr,obs}$	Final estimated prompt emission duration from the simulation, corresponding to $T_{90}$ for real source
$T_{ce,obs}$	Observation inferred central engine timescale in the simulation, corresponding to $t_{burst}$ for real source
$T_{col,lab}$	Last mechanical collision time in lab frame during internal shock phase
$T_{eff,lab}$	Last effective collision time in lab frame during internal shock phase
$T_{col}$	$T_{col,lab}$ value in observer frame
$T_{eff}$	$T_{eff,lab}$ value in observer frame
$T_{af}$	Timescale for last identifiable internal signature in X-ray afterglow light curve
$t_{col}$	Collision time for two shell case in lab frame
$t_{col,obs}$	$t_{col}$ value in observer frame
$\delta t_e$	Emission duration for internal shock in lab frame
$\delta t_{obs}$	Emission duration for refreshed shock in observer frame
$t_{lab,0}$	Initial lab frame time in one simulation
$t_{lab,n}$	Lab frame time for the $n$ th collision
$t_{next}^n$	Time interval between $(n - 1)$ th and $n$ th collision in lab frame
$t_n$	Detection time of $n$ th collision by observer at luminosity distance $D_L$ in lab frame
$t_{obs,n}$	Timescale for $n$ th collision since detector trigger time in observer frame
$\delta t_{obs,n}$	Observer frame emission duration for $n$ th collision
$t_{obs,n\gamma}$	Time for last effective internal collision for $\gamma$ -rays in observer frame
$\delta t_{obs,n\gamma}$	Emission duration for last effective internal collision for $\gamma$ -rays in observer frame
$t_{obs,nX}$	Time for last effective internal collision for X-rays in observer frame
$\delta t_{obs,nX}$	Emission duration for last effective internal collision for X-rays in observer frame
$t_{obs,nR}$	Time for last effective refreshed collision in observer frame
$\delta t_{obs,nR}$	Emission duration for last effective refreshed collision in observer frame
$\Delta t_{ej}$	Ejection time intervals between shells
$T_{quie}$	Time intervals between shells injection episodes

Table 1: Notation list for different timescales showing in this work.

Model	$\gamma$	$\Delta t_{\text{ej}}$ (s)	Episode	$T_{\text{quie}}$ (s)	$\log_{10}(m)$ (g)	$l/c$ (s)	Figure
1	RAN (50,500)	RAN (0.5,2.5)	1	---	RAN (27,29)	RAN (0.1,0.5)	1a, 1b
2	RAN (500,1000)	RAN (0.5,2.5)	1	---	RAN (27,29)	RAN (0.1,0.5)	1c, 1d
3	RAN (50,500)	RAN (5,25)	1	---	RAN (27,29)	RAN (0.1,0.5)	1e, 1f
4	PL (50,500,-1)	RAN (0.5,2.5)	1	---	RAN (27,29)	RAN (0.1,0.5)	1g, 1h
5	PL (50,500,-0.5)	RAN (0.5,2.5)	1	---	RAN (27,29)	RAN (0.1,0.5)	--
6	PL (50,500,-0.1)	RAN (0.5,2.5)	1	---	RAN (27,29)	RAN (0.1,0.5)	--
7	PL (100,500,-0.5)	RAN (0.5,2.5)	1	---	RAN (27,29)	RAN (0.1,0.5)	1i, 1j
8	PL (100,500,-0.5)	RAN (5,25)	1	---	RAN (27,29)	RAN (0.1,0.5)	--
9	GAUSS (300,100)	RAN (0.5,2.5)	1	---	RAN (27,29)	RAN (0.1,0.5)	1k, 1l
10	GAUSS (300,100)	RAN (5,25)	1	---	RAN (27,29)	RAN (0.1,0.5)	--
11	RAN (50,500)	RAN (0.5,2.5)	2	$10^3$	RAN(27, 29), RAN(27, 29)	RAN (0.1,0.5)	1m, 1n
12	RAN (50,500)	RAN (0.5,2.5)	2	$10^3$	RAN(27, 29), RAN(25, 27)	RAN (0.1,0.5)	1o, 1p
13	RAN (50,500)	RAN (0.5,2.5)	2	$10^4$	RAN(27, 29), RAN(27, 29)	RAN (0.1,0.5)	--
14	RAN (50,500)	RAN (0.5,2.5)	2	$10^4$	RAN(27, 29), RAN(25, 27)	RAN (0.1,0.5)	--
15	PL (100,500,-0.5)	RAN (0.5,2.5)	2	$10^3$	RAN(27, 29), RAN(27, 29)	RAN (0.1,0.5)	--
16	PL (100,500,-0.5)	RAN (0.5,2.5)	2	$10^3$	RAN(27, 29), RAN(25, 27)	RAN (0.1,0.5)	--
17	PL (100,500,-0.5)	RAN (0.5,2.5)	2	$10^4$	RAN(27, 29), RAN(27, 29)	RAN (0.1,0.5)	--
18	PL (100,500,-0.5)	RAN (0.5,2.5)	2	$10^4$	RAN(27, 29), RAN(25, 27)	RAN (0.1,0.5)	--
19	GAUSS (300,100)	RAN (0.5,2.5)	2	$10^3$	RAN(27, 29), RAN(27, 29)	RAN (0.1,0.5)	--
20	GAUSS (300,100)	RAN (0.5,2.5)	2	$10^3$	RAN(27, 29), RAN(25, 27)	RAN (0.1,0.5)	--
21	GAUSS (300,100)	RAN (0.5,2.5)	2	$10^4$	RAN(27, 29), RAN(27, 29)	RAN (0.1,0.5)	--
22	GAUSS (300,100)	RAN (0.5,2.5)	2	$10^4$	RAN(27, 29), RAN(25, 27)	RAN (0.1,0.5)	--

Table 2: Collection of different initial conditions for the simulation and figure numbers corresponding to different models. For one episode cases,  $T_{\text{ej}}$  is in order of 100 s (1000 s) when  $\Delta t_{\text{ej}}$  is distributed as RAN(0.5, 2.5) (RAN(5,25)). For two episode cases,  $T_{\text{ej}}$  is essentially determined by  $T_{\text{quie}}$ .

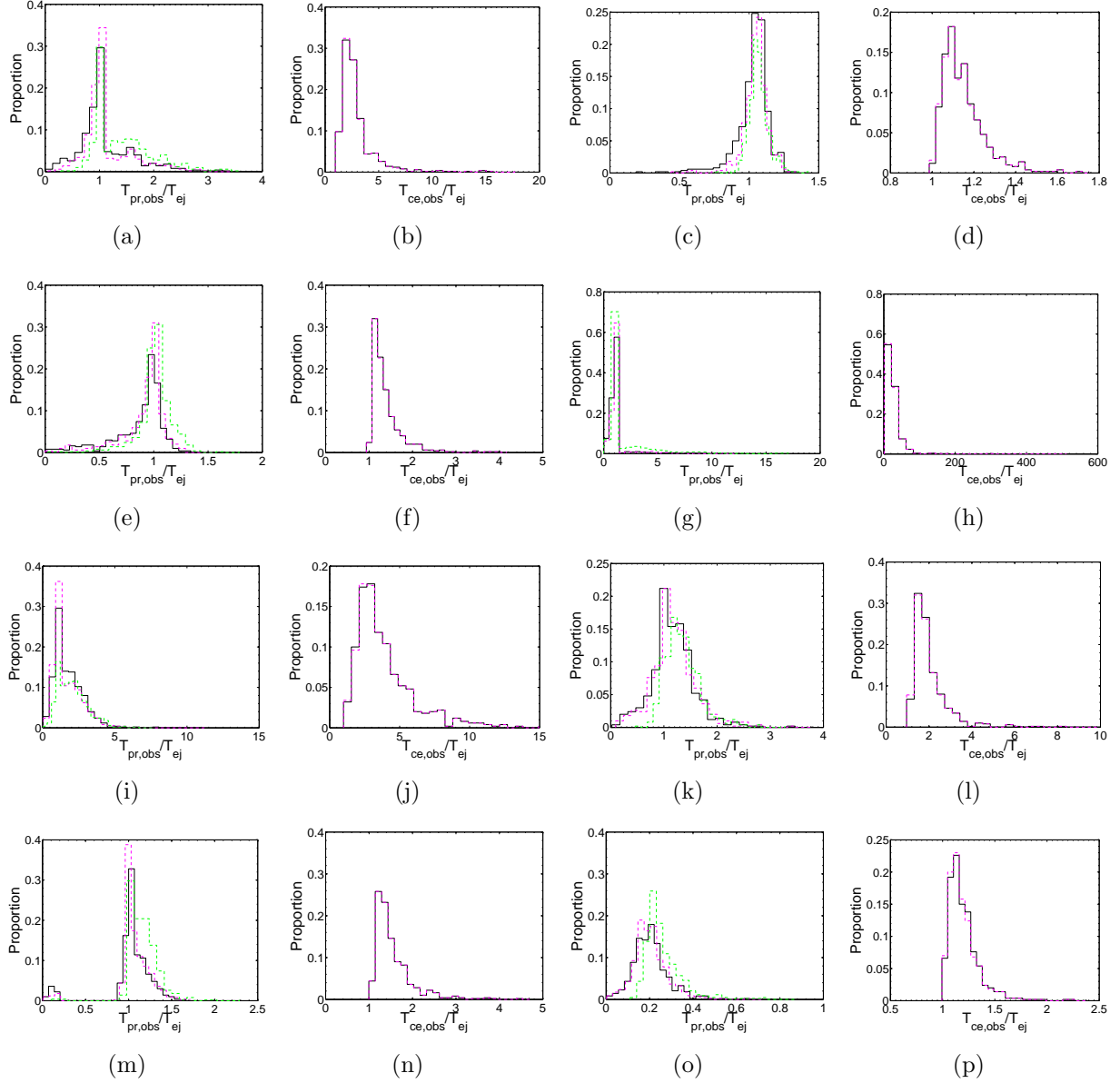


Fig. 1.— Distributions of  $T_{pr,obs}/T_{ej}$  and  $T_{ce,obs}/T_{ej}$  for selected models. The corresponding models for each subfigure are summarized in Table 2. Black lines are for  $L_{det,\gamma} = 10^{-8}$  erg s $^{-1}$  cm $^{-2}$  and  $f = 0.5$ ; pink lines are for  $L_{det,\gamma} = 10^{-8}$  erg s $^{-1}$  cm $^{-2}$  and  $f = 1$ ; green lines are for  $L_{det,\gamma} = 10^{-9}$  erg s $^{-1}$  cm $^{-2}$  and  $f = 1$ .

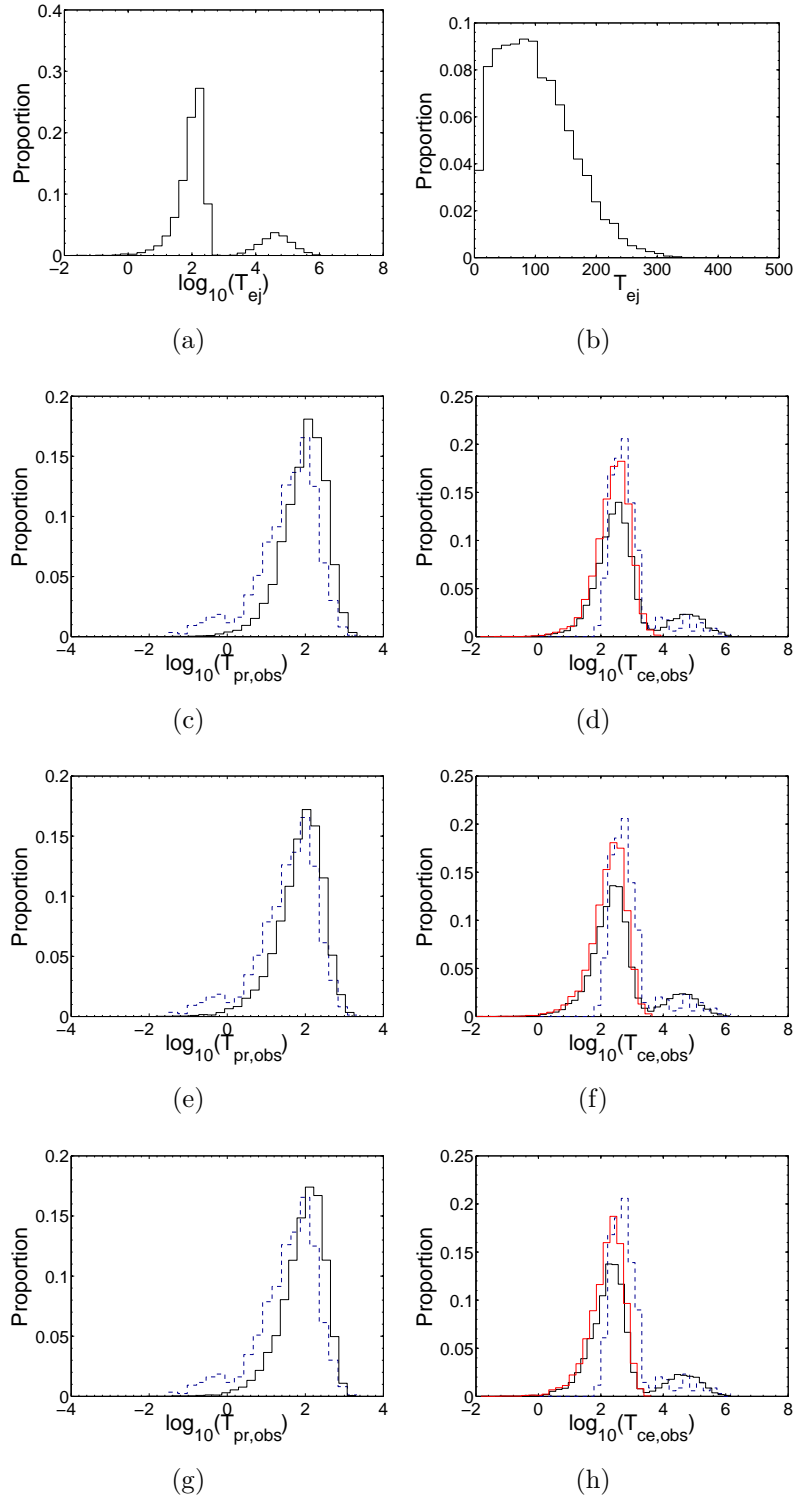


Fig. 2.— An example of a  $T_{ce}$  ( $T_{ej}$ ) distribution that gives reasonable results for both  $T_{90}$  ( $T_{pr,obs}$ ) and  $t_{burst}$  ( $T_{ce,obs}$ ). (a) distribution of  $T_{ej}$  in log space; (b) distribution of first component for  $T_{ej}$  in linear space;  $T_{pr,obs}$  and  $T_{ce,obs}$  distributions for (c-d) RAN-type  $\gamma$  initial condition, (e-f) PL-type  $\gamma$  initial condition, and (g-h) GAUSS-type  $\gamma$  initial condition. Solid and dash lines represent simulation results and observational data respectively. Red solid lines are for the results without considering the second component for  $T_{ej}$ .